AIAA JOURNAL
Vol. 47, No. 6, June 2009

Flowfield Downstream of Circular Cylinders Immersed Within Thick Boundary Layers

John M. Davis* and Norman Toy†
Engineering and Scientific Innovation, Inc., Blue Ash, Ohio 45241
and
Peter J. Disimile‡
University of Cincinnati, Cincinnati, Ohio 45221-0070

DOI: 10.2514/1.36085

With little data currently available, designers of physical models of aircraft engine nacelles have little basis to determine the size of geometric detail required to provide a sufficient representation of the actual specimen. The current study presents an experimental investigation into the minimum geometry size required for accurate aircraft engine simulator design by measuring the turbulent shear flow downstream of two-dimensional surface-mounted circular cylinders of various sizes. Cylinder diameters D of 5, 10, 20, and 40 mm were individually flush-mounted on the test-section floor of a wind tunnel specifically designed to simulate an aircraft engine nacelle, which operated at a freestream velocity and turbulence intensity of 8.4 m/s and 1%, respectively. The turbulent boundary layer approaching each cylinder had a thickness δ_{99} of 39 mm, yielding examined δ_{99}/D ratios of 0.98, 1.97, 3.93, and 7.86. Velocity profiles were measured using hot-wire anemometry at several locations downstream of each cylinder. The results showed that the separated shear-layer location was observed to significantly differ from that reported for sharp-edged obstructions, with the shear layer maintaining a constant height for δ_{99}/D ratios of 3.93 and 7.86.

Nomenclature

C_d	=	drag coefficient
c_f	=	skin-friction coefficient
D	=	cylinder diameter, mm
E	=	constant-temperature-anemometry uncorrected voltage output, V
E_{corr}	=	temperature-corrected constant-temperature-anemometry voltage, V
H	=	boundary-layer shape factor
h	=	test-section height, mm
m	=	constant-temperature-anemometry sensor-temperature loading factor
T_a	=	constant-temperature-anemometry acquisition temperature, K
T_o	=	constant-temperature-anemometry calibration temperature, K
T_w	=	constant-temperature-anemometry hot-wire sensor temperature, K
U_∞	=	freestream average streamwise velocity at each measurement location, m/s
$U_{\infty o}$	=	undisturbed freestream average streamwise velocity, m/s
u	=	local average streamwise velocity, m/s
u^*	=	wall-friction velocity, m/s
u'	=	local streamwise fluctuating velocity, m/s
X_r	=	reattachment location, mm
x	=	streamwise direction
y	=	vertical direction (across test-section height)
z	=	lateral direction (across test-section width)
β	=	area blockage ratio, D/h
δ_s	=	width of the separated shear layer, mm
δ_ω	=	shear-layer vorticity thickness, mm
δ_{99}	=	reference boundary-layer thickness, mm
δ^*	=	reference boundary-layer displacement thickness, mm
θ	=	reference boundary-layer momentum thickness, mm

Received 20 May 2008; accepted for publication 18 January 2009.

*Research Engineer, 4625A Carlyn Drive; jdavis@esi-solutionsinc.com. Member AIAA.
†Chief Engineer; dr.toy@esi-solutionsinc.com.
‡Associate Professor, Department of Aerospace Engineering, 480 Education and Research Center, P.O. Box 210070. Senior Member AIAA.

Introduction

AIRCRAFT engine nacelles present a complex problem in fire-suppression studies, due to a large amount of obstructions (or clutter) within a confined space. Adding further to the problem is the highly turbulent airflow associated with aircraft engine nacelles. Because of the high cost of production aircraft, much of the test and evaluation (T/E) of fire-suppression systems has been performed using generic ground-based simulators. These simulators are meant to provide a means for fire-suppression system T/E in a repeatable and cost-effective manner. Full-scale simulators (geometric approximations to actual aircraft components) are often fabricated for fire-testing, with their cost directly related to the size and material of the test article and the level of geometric detail needed to ensure an accurate representation of a given platform. Currently, detail is only given to salient geometric features such as large ribs or spars, main fuel lines, wire bundles, etc., whereas small spars, surface protrusions, individual hydraulic or fuel lines, standoffs, etc., are usually neglected. Although this strategy may have minimal impact on fire tests in the absence of airflow through the nacelle, in the presence of airflow, these elements could substantially alter the T/E outcome. This brings into question the existence of a minimum-size requirement for geometric detail, in which an accurate representation of the actual platform is still provided, but simulator cost is minimized by omitting details that are smaller than the minimum.

The study of airflow over the complex geometry found within aircraft engine nacelles can be broken down into three main categories: obstructions in the freestream, surface-mounted obstacles, and obstacles within the wall boundary layer but not surface-mounted. Each of these categories may be further divided into sharp-edged clutter and smooth-edged clutter. Although both two- and three-dimensional obstructions reside within engine nacelles, most three-dimensional clutter elements have relatively high aspect ratios; thus, the airflow around engine nacelle clutter may be represented in a two-dimensional sense. Breaking down the complex

geometry of an aircraft engine nacelle into generic geometries and studying the various effects that these geometries pose on the airflow will increase the knowledge base required to give justification for the level of geometric detail required in the fabrication of generic aircraft engine nacelle simulators.

Although the wakes created by freestream obstructions have been extensively studied and are somewhat fundamental, obstacle interaction with a boundary layer, whether the obstacle is surface-mounted or suspended above the floor, is much less documented. Unfortunately, a majority of clutter found within aircraft engine nacelles falls under this scenario of obstacle/boundary-layer interaction, with the most common being of the surface-mounted type. Furthermore, surface-mounted geometries are also the most complex for airflow studies, as they contain characteristics of both a forward- and backward-facing step. The complexity of this scenario is best described by Bradshaw and Wong [1], who classified it as an overwhelming permutation in which the incoming shear layer (in this case, the wall boundary layer) is completely changed by the obstruction into a different type of shear layer, such as a separated shear layer and mixing layer.

The study of airflow over surface-mounted two-dimensional obstructions has been mainly focused on sharp-edged objects, for which the point of separation is at a constant location. For example, studies by Bergeles and Athanassiadis [2], Ke et al. [3], and Archaya et al. [4] experimentally examined the wake downstream of two-dimensional rectangular prisms of constant height; thus, a constant δ_{99}/D and β was maintained. In more recent research efforts, Abdalla et al. [5] and Hwang et al. [6] presented numerical studies that showed good agreement with the experimental data of Bergeles and Athanassiadis [2] and Archaya et al. [4], thereby demonstrating a recent shift toward the turbulence modeling of airflow over sharp-edged obstructions.

Of the currently available literature on sharp-edge surface-mounted obstructions, only a few studies have been conducted in which the effect of obstruction size was investigated. Atli [7] presented a study examining the airflow around vertical sharp-edged fences with δ_{99}/D ratios of 1.0, 1.7, 2.5, and 5.0, concluding that the downstream reattachment point was unsteady and reattachment occurred earlier for increasing δ_{99}/D. Furthermore, Atli concluded that the maximum turbulence level in the separated shear layer increased as δ_{99}/D decreased and Re_D increased. The effects of blockage on the shear-layer location and growth downstream of vertically mounted sharp-edged fences of various sizes was investigated by Castro and Fackrell [8], who found that the effect of area blockage is complex due to the fact that the upstream boundary layer is completely changed. For ratios of boundary-layer thickness to obstruction height (δ_{99}/D) larger than 2.3, the effect of β on the reattachment length is only slight, whereas for ratios less than 2.3, increasing β decreases the reattachment length.

Although several studies have investigated the airflow around sharp-edged surface-mounted obstructions, information on two-dimensional boundary-layer obstructions with highly curved surfaces is much more sparse. One of the only three studies that specifically investigated the airflow around a two-dimensional surface-mounted circular cylinder was conducted by Aragaki et al. [9], who presented a theoretical examination of the flow over a surface-mounted circular cylinder under a constant β of 13%. In that study, the authors compared theoretical values of the downstream reattachment lengths to two experimental investigations on circular cylinders (published in Japanese) and stated that the experimental data suggested that the reattachment length is relatively constant between 6.9 and 8.7 cylinder diameters for Re_D greater than 2500. However, all three studies only accounted for a single δ_{99}/D and β; thus, to the authors' knowledge, no information is currently available that specifically examines the combined effect of β, δ_{99}/D, and Re_D on the shear layer separating from surface-mounted two-dimensional highly curved obstructions.

The current investigation aims to investigate the airflow downstream of highly curved two-dimensional surface-mounted obstructions of varying sizes in duct flows similar to aircraft engine nacelles. To achieve this, airflow velocity measurements were acquired downstream of two-dimensional circular cylinders, which were surface-mounted and immersed within the turbulent wall boundary layer of a wide–narrow wind tunnel that was specifically designed to simulate an aircraft engine nacelle flow. Four different cylinder diameters were examined under a constant inflow boundary condition, thereby providing an investigation into the combined effect of δ_{99}/D, β, and Re_D on the shear layer as it separates from cylindrical obstructions.

Experimental Arrangement

An experimental facility designed specifically to simulate airflow in typical aircraft engine nacelles in a two-dimensional sense was used for the current investigation. This facility operates at a high flow rate and elevated degree of nonuniformity, which is typical of aircraft engine nacelle flows, as described by Black et al. [10]. This facility is a single-speed open-loop wind tunnel operated in a blowdown arrangement (Fig. 1) and contains three major components: blower, diffuser, and test section. Air is drawn from a large laboratory by a centrifugal blower and decelerated through a wide-angle diffuser into a wide but narrow test section, which is then exhausted back into the laboratory. The test section was designed to be geometrically similar to an unfolded annulus and has a width of 183 cm, a height of 23 cm, and a length of 244 cm. Flow conditioning was conducted in the diffuser using a combination of turning vanes, screens, and honeycomb to achieve a uniform two-dimensional airflow with a freestream velocity variation of less than ±6% across the center 55% of the test section.

Solid smooth-steel circular cylinders with diameters of 5, 10, 20, and 40 mm and lengths that spanned the entire width of the test section were installed flush to the test-section floor. Special care was taken to ensure that no air leaked beneath the clutter by sealing the contact surface between the floor/clutter with a polymer-based

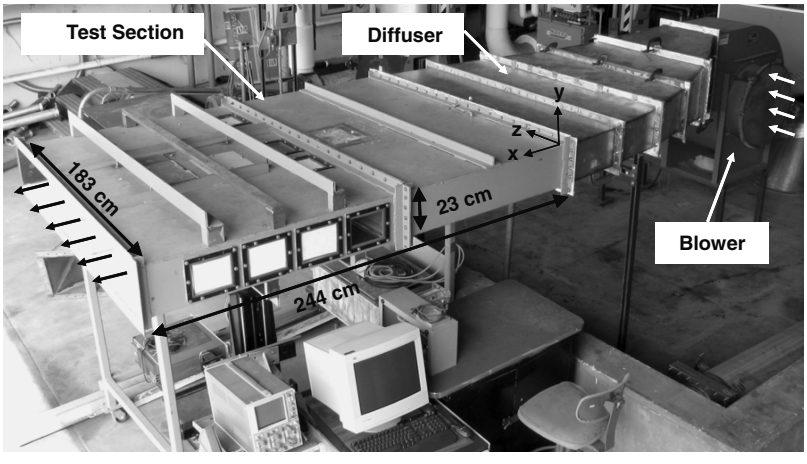

Fig. 1 Test facility.

sealant. The leading edge of each clutter element was installed 1200 mm downstream of the test-section inlet, which allowed sufficient development in the approaching boundary layer. Cylinder diameters were selected to cover blockage ratios of $\beta = 2$ to 17% and boundary-layer thickness ratios of $\delta_{99}/D = 0.98$ to 7.93.

For each test case, a single cylinder was installed flush with the test-section floor, and velocity measurements were acquired across the y axis and on the test-section width centerline ($z = 0$) at 1, 2, 4, and 6D downstream of the cylinder (Fig. 2). As shown in Fig. 2, the airflow approaching the cylinder separates from the test-section floor immediately upstream of the cylinder, impacts the cylinder, then separates from the cylinder surface, thereby changing from a surface-bound shear layer to a free shear layer. The free shear layer then reattaches to the test-section floor at some distance downstream of the cylinder noted by X_r, thus forming a recirculation region downstream of the cylinder. For each of the four cases, X_r was found to be greater than 6D; therefore, all downstream velocity traverses were conducted before reattachment of the free shear layer.

Experimental Strategy

Streamwise velocity surveys were conducted across the y axis along the center of the test section ($z = 0$), both upstream and downstream of each individual cylinder under a constant average test-section airspeed. All velocity measurements were acquired using a single-channel constant-temperature-anemometry (CTA) system, which consisted of the following components: a single-sensor 5 μm tungsten hot-wire probe, a Dantec 55M01 anemometer, and a Dantec 55M10 standard bridge. A miniature k-type bare-bead thermocouple was mounted to the side of the CTA probe to monitor any temperature fluctuations that would influence the CTA data. Both CTA and thermocouple measurements were simultaneously sampled using a high-speed analog-to-digital data conversion and acquisition system. Measurements were acquired for 18 s at a rate of 25 kHz for each location in the velocity survey. This data sampling rate and duration were selected based on pretest results, which showed that 25 kHz was sufficiently fast to resolve the flowfield fluctuations, and a duration of 18 s was well beyond that required for stationary averages. Probe positioning was accomplished using a micro-stepping computer-controlled traverse.

The airflow condition was first documented at the cylinder installation location ($x = 1200$ mm) in the absence of the cylinders, thus providing an undisturbed reference boundary condition. To resolve the upstream boundary-layer profile from the buffer region ($5 < y^+ < 30$) to well beyond the boundary-layer wake (i.e., free-stream), velocity measurement traverses were initiated at a position 0.25 mm above the test-section floor ($y = 0.25$ mm) and extended to $y = 120$ mm. To examine flow development, boundary-layer measurements were repeated at $x = 1320$ and 1440 mm. All velocity surveys performed downstream of the clutter elements were also initiated at $y = 0.25$ mm and were variably spaced through the separated shear layer and into the freestream.

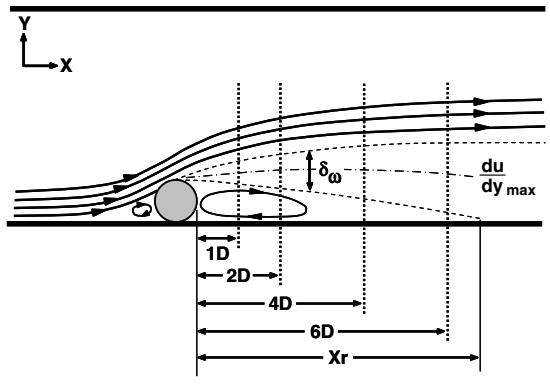

Fig. 2 Flowfield schematic.

Because of laboratory temperature variations, all CTA data were temperature-corrected before any additional data analysis using Eq. (1). Complete details of the temperature-correction procedure are listed in [11]. A loading factor of $m = 0.25$ was chosen for the current study, which is typical for single-sensor CTA hot-wire probes:

$$E_{\text{corr}} = E \cdot \left(\frac{T_w - T_o}{T_w - T_a}\right)^{0.5\cdot(1\pm m)} \tag{1}$$

Experimental Uncertainty

Two basic measurement uncertainties exist in the current program: uncertainty in the hot-wire measured velocity and uncertainty in the hot-wire measurement position. The uncertainty in the measurement position was a combination of the uncertainty in the initial positioning of the hot-wire probe and the uncertainty in the traverse movement. The hot-wire probe was carefully positioned using a surveyor's transit and calibrated shims to an accuracy of 0.06 mm, and the microstepping traverse provided an accuracy of 0.02 mm; therefore, the overall uncertainty in the probe position Δy was equal to ± 0.08 mm. The uncertainty in the hot-wire measured velocities Δu is a combined effect of uncertainties in the probe calibration, temperature correction, and misalignment of the hot-wire probe and the flow direction. The combined uncertainty in the probe calibration and temperature-correction procedure was found to be $\pm 2\%$; however, the main component of uncertainty in u is due to probe/flow direction misalignment.

The primary uncertainty in u arises from the response of a single hot-wire probe to two-dimensional flow vectors that are nonnormal to the sensing element: namely, streamwise (x axis, normal to the hot wire) and cross-stream (y axis). Because the hot-wire probe was aligned parallel to the z axis, the influence of flow across the z axis (spanwise) is negligible, due to the relative insensitivity of the probe to spanwise flow. Therefore, only the pitch response of the hot-wire will influence the current data. As described by Jorgensen [12], a single pitched ideal hot wire responds by the cosine law to the two-dimensional flow vector, with the measured velocity equal to the vector addition of the cross-stream and streamwise velocities. However, due to end effects and the influence of the probe prongs, the actual response of a hot-wire deviates from the cosine law, thereby resulting in a measured velocity that is higher than the true velocity-vector magnitude At relatively small flow angles, the streamwise velocity will be dominant, with only a small cross-stream influence [12,13]. Flow-visualization analysis was conducted for each clutter element to examine the maximum flow angle to determine the influence of the cross-stream flow on the hot-wire velocities. Through careful analysis, it was found that the maximum flow deflections occurred for the 40 mm clutter, with a maximum deflection angle of 14 deg from parallel to the x axis measured at 1D downstream of the clutter. This flow angle decreases to 9 deg at 2D downstream of the clutter and further to 5 and 3 deg at the 4D and 6D locations. Maximum flow deflection angles of less than 10 deg were observed for the remaining clutter sizes, with the maximum flow deflection always occurring at 1D downstream of the clutter. With a maximum flow deflection angle of 14 deg, and following the response analysis in [12,13], the maximum difference of the measured velocity and the actual streamwise velocity is 3%. Therefore, the combined maximum uncertainty in the hot-wire velocity data Δu is $\pm 5\%$. Although the uncertainty in Δu is reported as $\pm 5\%$, note that this is a maximum uncertainty and is only present for measurement locations in the shear layer at 1D downstream of the 40 mm clutter element. Velocity measurements outside of this region will contain an uncertainty between 2 and 4%.

The remaining quantities presented in the current paper are all derived from the velocity and probe position. Therefore, the uncertainty of each derived value was computed using uncertainty-propagation analysis. The uncertainties in the measured data and all derived data presented herein are listed individually in Table 1. The maximum uncertainties in u and y of $\pm 5\%$ and ± 0.08 mm were used to calculate all derived values listed in Table 1.

Table 1 Experimental uncertainties

Parameter	Δu	Δy	$\Delta\delta_\omega$	$\Delta\delta_{99}$	$\Delta\delta^*$	ΔH	Δc_f	Δu^*	ΔC_d	ΔX_r
Uncertainty	±5%	±0.08 mm	±8%	±0.02 mm	±6%	±10%	±1%	±5%	±11%	±1D

Results

The results are shown next in three subsections. The upstream boundary-layer measurements are presented in the first section, which provides the baseline documentation by which the cylinders were installed, and all downstream measurements are presented in the second section. The final section presents results on the combined effects of the ratios of blockage and boundary layer to cylinder diameter.

Upstream Boundary-Layer Characterization

The reference boundary-layer velocity and turbulence-intensity (T.I.) profiles are shown in Fig. 3, and the corresponding boundary-layer parameters are shown in row 1 of Table 2. All of the quantities shown in Table 2 were directly computed from the velocity measurements, including the skin-friction coefficient, which was calculated using the method outline by Clauser [14]. The boundary-layer quantities measured at $x = 1440$ mm are also included in row 2 of Table 2 for examination of flow development. The facility freestream airspeed varied day to day and was found to have an average of 8.4 m/s ± 6% and an average T.I. of 0.01 ± 0.002 in the freestream. This corresponds to Reynolds numbers (based on the undisturbed freestream velocity and the cylinder diameter) of 2.8×10^3, 5.5×10^3, 1.1×10^4, and 2.2×10^4 for the 5, 10, 20 and 40 mm cylinders, respectively.

To analyze the developmental stage of the reference boundary layer, the velocity profile shown in Fig. 3 was plotted using the inner-law variables $u+$ and $y+$ and was fit with the universal log law of the wall, as shown in Fig. 4. Using a roughness factor of 5.44, the velocity profile fits the law of the wall for $y+$ values between approximately 25 and 250, thereby covering a decade. Combining this with a measured shape factor of 1.38 shows that the boundary layer at $x = 1200$ mm can be considered to be a fully developed turbulent boundary layer. This fact is further supported by comparing the boundary-layer quantities listed in Table 2 for the boundary layers measured at $x = 1200$ and 1440 mm, in which all the listed quantities are within experimental uncertainty.

The circular cylinders are pictorially represented in Fig. 3, and the location of the top edge of each cylinder is shown as points in Fig. 4 to provide an indication of each of the cylinder sizes to the upstream reference boundary layer. From these two figures, it may be seen that the 5 and 10 mm cylinders reside deep within the reference boundary layer, with their top edge located within the law-of-the-wall region, in which high shear occurs. The 40 mm cylinder is on the order of the reference boundary-layer thickness; thus, its top edge is at a location in which the shear is close to freestream quantities, and the 20 mm cylinder resides within the wake region of the reference boundary layer, with the top edge of the cylinder located in a region of shear between that of the 40 and 10 mm cylinders.

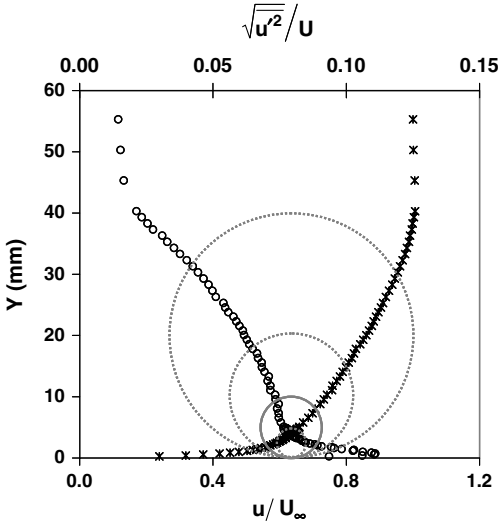

Fig. 3 Reference boundary-layer velocity and turbulence-intensity profiles.

Note that the presence of the obstructions will undoubtedly affect the approaching boundary layer. However, documentation of the disturbed boundary layer is beyond the scope of the current investigation and is therefore not included. Furthermore, documentation of the undisturbed boundary layer is more appropriate for simulator design purposes in which the incoming airflow is known but the obstruction size is not.

Downstream Measurements

Velocity and turbulence-intensity profiles for the four δ_{99}/D ratios are shown in Figs. 5–12. All profiles are plotted nondimensionally, with the individual freestream velocity U_∞ used to normalize the plotted quantity. That is, the freestream velocity for each profile was used to normalize any given profile, rather than using the undisturbed freestream velocity measured without any obstruction installed. Each figure includes the four profiles measured at each x/D location, which are plotted against y normalized by δ_{99}. Although it is customary to normalize the vertical location by the surface-mounted obstruction height, normalizing by the boundary-layer thickness is more appropriate for the current investigation, because it provides a clearer representation of the clutter size in relation to the upstream boundary-layer thickness. In addition, the upstream reference boundary-layer profile is plotted as a solid line at each downstream location for direct comparison with the downstream measurements (open symbols).

Although measurements were acquired at spatial locations that extend through the free shear layer and into the flow recirculation region downstream of the clutter, the data acquired within the flow-reversal area of the downstream recirculation region cannot be trusted, because the CTA technique used cannot distinguish between flow directions. Because the focus of the current study is to characterize the flow within the free shear layer separating from the cylinder, not the reversed flow section of the downstream recirculation region, measurements below the center of recirculation region (indicated by the minimum velocity) have been ignored and omitted from the present data.

The shear-layer center (dashed–dotted curve in Figs. 5–12) was calculated from the velocity data and is defined as the location of the maximum velocity gradient $\mathrm{d}u/\mathrm{d}y_{\max}$. The velocity gradient was calculated by differentiating a sixth-order polynomial fit to the velocity profiles, which was found to have a fit-correlation coefficient greater than 0.99 in all cases. The shear-layer upper and lower edges were then computed by calculating the vorticity thickness of the shear layer, δ_ω, and assuming symmetry about the shear center. The dashed curves shown in Figs. 5–12 were therefore calculated by adding and subtracting half of the shear-layer vorticity thickness from the shear-layer center location. The shear-layer vorticity thickness is defined in Eq. (2) [15]:

$$\delta_\omega = (U_{\max} - U_{\min}) \Big/ \frac{\mathrm{d}u}{\mathrm{d}y_{\max}} \tag{2}$$

Note that in a mixing layer between two streams with well-defined constant velocity profiles, the maximum and minimum velocities in Eq. (2) are the asymptotic values in the velocity profiles between the two streams. However, for the current investigation, the separating shear layer is immersed within a shear layer itself (upstream boundary layer); thus, the velocity profile above the cylinder edge

Table 2 Reference boundary-layer and freestream quantities

x, mm	$U_{\infty o}$, m/s	T.I.$_{\infty o}$	δ_{99}, mm	δ^*, mm	θ, mm	H	c_f	u^*, m/s
1200	8.4	0.01	38.3	6.9	5.0	1.38	0.003	0.34
1440	8.0	0.01	39.3	6.7	5.0	1.34	0.0032	0.34

does not immediately approach the freestream velocity at the edge of the separated shear layer. Rather, the velocity gradually asymptotes into the upstream shear profile, which then gradually approaches the freestream. Therefore, with such a complex situation, care must be taken when determining the vorticity thickness: namely, the region for which the maximum and minimum velocity will be chosen. This effect is best illustrated in Fig. 5, in which a dramatic increase in the velocity profiles is observed between y/δ_{99} of 0.1 and 0.3, which is the effect of the separated shear layer. However, at y/δ_{99} of 0.3, the velocity profile is not at a maximum and continues to increase and approach the freestream, which is an effect of the upstream shear layer. Therefore, if the maximum velocity were taken as the freestream for this case, the vorticity thickness would partially include the thickness of the upstream shear layer, which would yield δ_ω values larger than the actual separated shear-layer thickness. Thus, the maximum and minimum velocity used to calculate δ_ω for this case were chosen to be between y/δ_{99} of 0.1 and 0.3. This calculation method was also used for the remaining three cylinders, as appropriate.

The presence of the cylinder appears to have a similar general effect on the incoming airflow, regardless of the cylinder size (as seen in Figs. 5–12). That is, the velocity is at a minimum value behind the cylinder, which then increases to velocities slightly higher than the reference boundary-layer profile, then gradually decreases to match that of the reference boundary-layer profile. The turbulence-intensity profiles are observed to have maximum values occurring at the shear-layer center, with gradual decreases toward the shear-layer edges. However, the cylinder's effect on the turbulence-intensity profiles was observed to cover a larger area than its effect on the mean velocity. Although the turbulence intensity reaches a minimum at the lower shear-layer edge, the turbulence intensity does not return to reference boundary-layer-profile values at the upper shear-layer edge. Instead, the turbulence intensity remains at values higher than the reference boundary layer until well beyond the reference boundary-layer thickness. This may be observed in Fig. 10, in which the upper shear-layer edge is located at y/δ_{99} of 0.8, and the turbulence intensity does not return to the reference boundary-layer values until y/δ_{99} of 1.8. Furthermore, it was generally observed for all cases that as the separated shear layer propagates downstream, it increases in width, which in turn gradually decreases the difference between velocity at the upper and lower edges of the shear layer and spreads the turbulence-intensity profiles without any reduction in turbulence-intensity values.

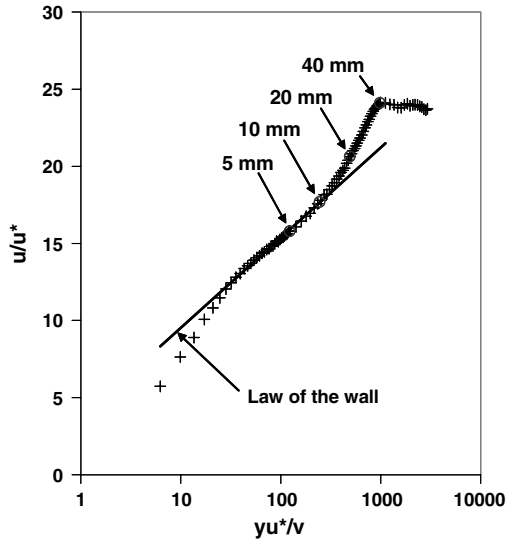

Fig. 4 Reference boundary-layer plotted using inner-law variables.

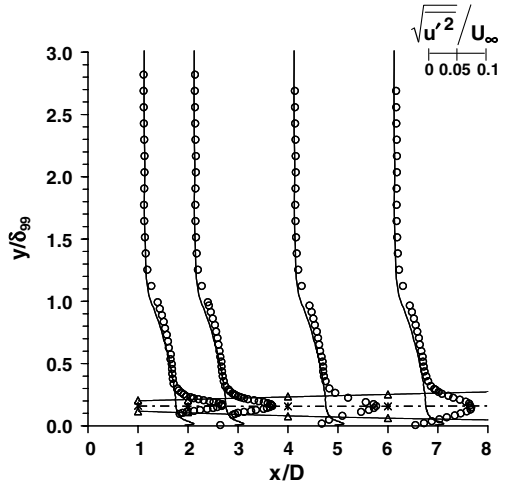

Fig. 6 Streamwise turbulence-intensity profiles, $\delta_{99}/D = 7.86$.

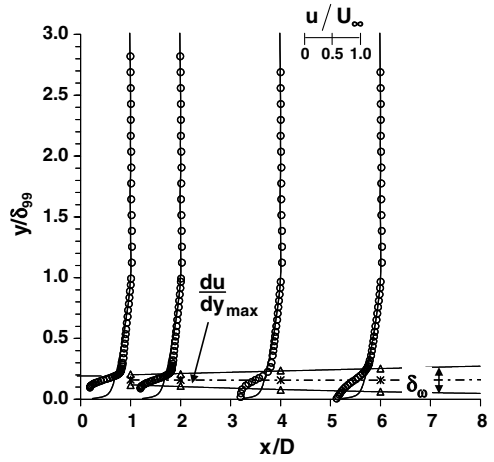

Fig. 5 Streamwise velocity profiles, $\delta_{99}/D = 7.86$.

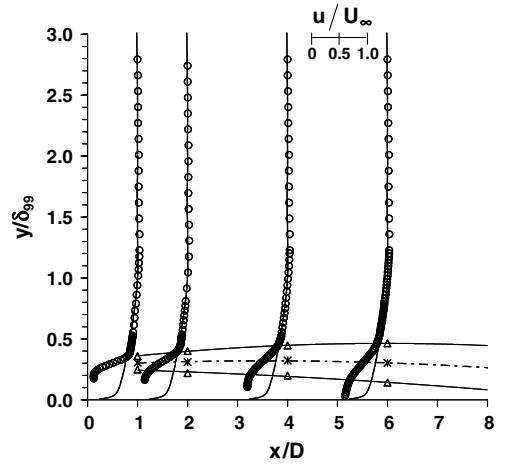

Fig. 7 Streamwise velocity profiles, $\delta_{99}/D = 3.93$.

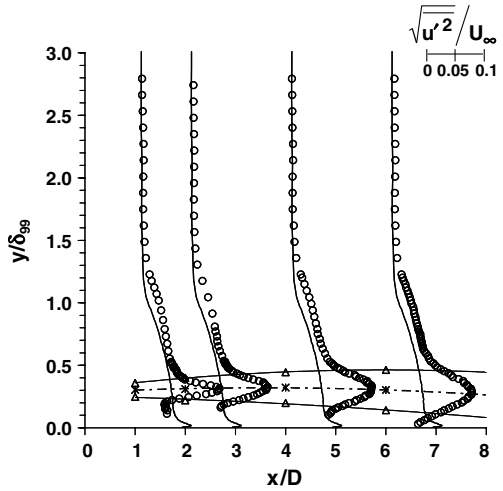

Fig. 8 Streamwise turbulence-intensity profiles, $\delta_{99}/D = 3.93$.

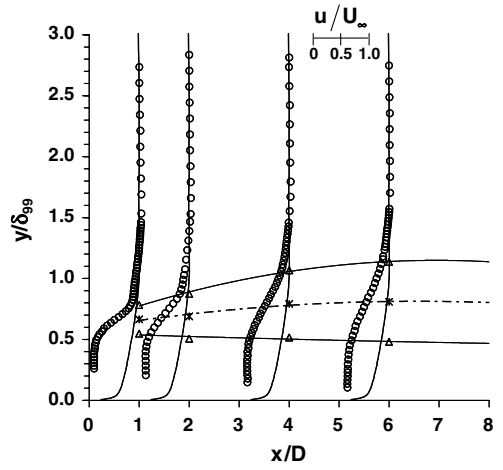

Fig. 9 Streamwise velocity profiles, $\delta_{99}/D = 1.97$.

Combined Results

The effect of blockage was investigated by calculating the drag coefficient for each cylinder (Table 3). Calculation of C_d was facilitated using the standard momentum-deficit method, with the reference boundary-layer velocity profile used as the upstream condition and the velocity profiles at $x/D = 6$ used for the downstream/wake condition. To allow direct comparison of the C_d values for each clutter element, the freestream velocity of the reference boundary layer was selected to normalize the drag values.

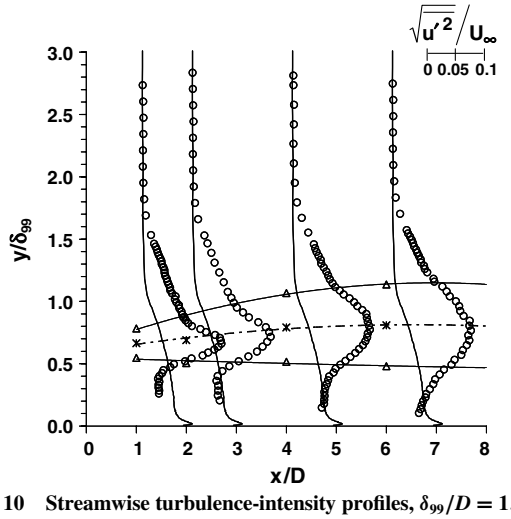

Fig. 10 Streamwise turbulence-intensity profiles, $\delta_{99}/D = 1.97$.

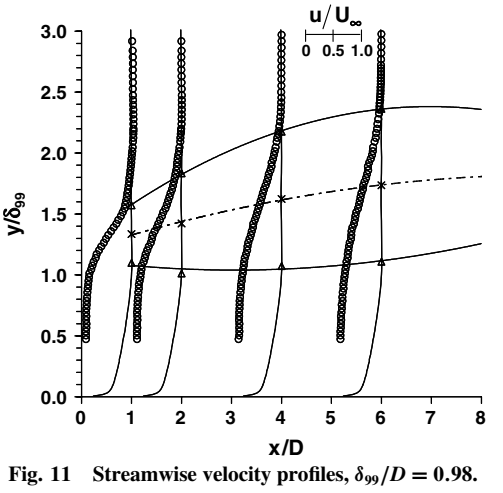

Fig. 11 Streamwise velocity profiles, $\delta_{99}/D = 0.98$.

From the data shown in Table 3, it may be observed that as δ_{99}/D increases (thus increasing β), C_d increases, with the exception of the 40 mm cylinder, in which a slight decrease was observed. The downstream reattachment lengths were also measured for each cylinder using cotton tufts and observing the location at which the flow reversed directions close to the test-section floor. Figure 13 shows the measured X_r values (normalized by D) plotted against δ_{99}/D, showing that X_r/D linearly decreases with increasing δ_{99}/D. Also plotted on Fig. 13 are the data presented by Atli [7] for sharp-edged fences, showing reasonable agreement in the downstream recirculation lengths.

The shear-layer vorticity thickness (normalized by D) was plotted against x/X_r in Fig. 14 for each δ_{99}/D ratio. Because X_r was found to be dependent on the cylinder size, the downstream location was normalized by each cylinder's recirculation length, which provides a more accurate representation of the physical flow condition than normalization by the cylinder diameter D.

From examination of Fig. 14, it may be observed that δ_ω is approximately $0.5D$ for all cases at $x/X_r = 0.1$ and increases logarithmically with increasing x/X_r. However, the rate at which δ_ω grows increases with decreasing δ_{99}/D ratio, with the exception of the largest cylinder ($\delta_{99}/D = 0.98$), which (due to blockage effects) has a smaller width than $\delta_{99}/D = 1.97$ at every downstream location.

Although normalizing x by X_r provides a more accurate representation of the flow, it is more practical for simulator design purposes to normalize x by the cylinder diameter D, as shown in Fig. 15. In this case, all four shear-layer vorticity thicknesses (shown in Fig. 14) collapse onto a near linear function of x/D (solid line in Fig. 15). Thus, when both δ_ω and x are normalized by the cylinder diameter, the shear-layer thickness is observed to have no functional

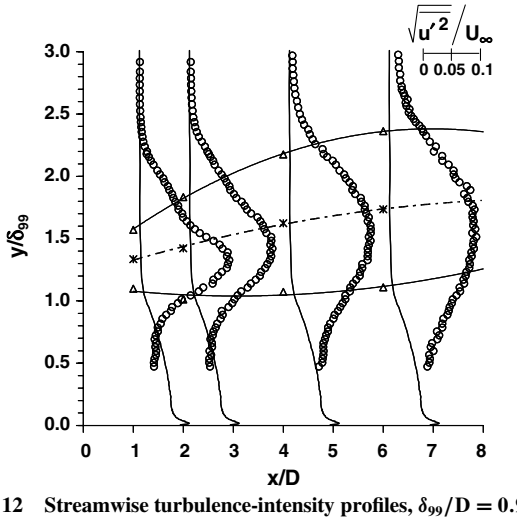

Fig. 12 Streamwise turbulence-intensity profiles, $\delta_{99}/D = 0.98$.

Table 3 Cylinder drag coefficients and reattachment lengths

D, mm	δ_{99}/D	β, %	C_d	X_r/D
5	7.86	2	0.27	7.8
10	3.93	4	0.51	10.2
20	1.97	9	0.75	11.7
40	0.98	17	0.71	12.9

dependence on the δ_{99}/D ratio and is only affected by the downstream location. The vorticity thickness spread rates reported by Brown and Roshko [16] and Viegas and Rubesin [17] are also included in Fig. 15 (dashed lines) for comparison purposes.

Although the shear-layer thickness was observed to be dependent only on x/D, the location of the shear-layer center showed dependency on both δ_{99}/D and x/D, as shown in Fig. 16. Here, the center of the shear layer for the four δ_{99}/D ratios was observed to fall into two groups: one for both δ_{99}/D equal to 7.86 and 3.93 (linear curve) and the other for δ_{99}/D equal to 1.97 and 0.98 (polynomial curve). In addition, a curve fit of the data presented by Atli [7] for sharp-edged fences with δ_{99}/D ratios of 1.0–5.0 is also included in Fig. 16 (dashed line) for reference.

From Fig. 16, it can be seen that the shear-layer center remained at a relatively constant height of approximately $1.2D$ at each x/D location for δ_{99}/D equal to 7.86 and 3.93. For the two larger cylinders, the shear-layer center location was observed to be initially at the same location as the smaller cylinders (at $x/\mathrm{D} = 1$), but increased to a height of approximately $1.6D$ at x/D of 6. Although Atli's [7] data were presented as the location of the maximum T. I., these data offer a direct comparison with the current data, because the maximum T.I. was found to occur within $\pm 5\%$ of the shear-layer center. Furthermore, Atli's data were found to be independent of δ_{99}/D and are thereby represented as a single polynomial fit. Comparison with the current data shows that the shear-layer center for sharp-edged fences follows roughly the same trend for the larger cylinders only, with the fence data reaching higher-y/D locations.

Discussion

When the 5 mm circular cylinder is deeply immersed within the approaching boundary layer ($\delta_{99}/D = 7.86$, where $D \sim \theta$), the top edge of the cylinder is beneath the displacement thickness of the reference boundary layer, falls on the law-of-the-wall region of the boundary layer, and is within a location of high shear (Figs. 3 and 4). Therefore, the shear layer that separates downstream of the cylinder is immersed within this high-shear region, thus suppressing the separating shear layer and causing it to remain at a relatively constant location with a center of $y/D \sim 1.2$ (Figs. 5 and 16). When δ_{99}/D is decreased to $3.93D$ (10 mm cylinder), the cylinder diameter is twice as thick as the approaching reference boundary-layer momentum thickness, approximately 40% larger than the displacement thickness, and falls on the edge of the law-of-the-wall region of the reference boundary layer. The shear layer separates from the 10 mm cylinder with nearly the same properties as the 5 mm cylinder (Figs. 15 and 16). Therefore, the similar separation phenomena must be occurring even when the cylinder diameter is twice the momentum thickness. This may be expected, due to the nature of the flow upstream of the cylinder, in which surface-mounted obstructions have been shown to increase the boundary-layer thickness immediately upstream of the obstruction [7,18]. Although documentation of the behavior of the flow upstream of the cylinder is beyond the scope of the current investigation, increases on the order of 30% have been previously documented for sharp-edged surface-mounted obstructions [7]; thus, it is likely that the top edge of the 10 mm cylinder is immersed within the displacement thickness of the thickened boundary layer immediately upstream of the cylinder (not the reference boundary), thereby resulting in a wake profile similar to that of the 5 mm ($\delta_{99}/D = 7.86$) case.

For the two cases in which the cylinder diameter is greater than twice the displacement thickness of the reference boundary layer (20 and 40 mm cylinders), the shear layer separates with a very different trajectory than that observed for the smaller cylinders. For the larger two cylinders, the shear-layer center is ramped upward and is highly dependent on the downstream location (Fig. 16). When the cylinder diameter is on the order of δ_{99} (40 mm cylinder), the airflow directly above the separated shear layer is close to freestream quantities (Figs. 11 and 12); thus, a lower level of shear stress may be expected. This allows the shear layer to freely separate from the cylinder with an upward displacement of the shear-layer center to a y/D location of 1.66 at 6 diameters downstream. However, this effect was also observed (although to a lesser extent) for the 20 mm cylinder, where $\delta_{99}/D = 1.97$, showing that even though the cylinder is within the upstream boundary-layer thickness, the level of shear due to the upstream boundary layer at the top edge of the 20 mm cylinder is relatively small and thus only slightly suppresses the upward deflection of the separated shear layer to a height of $1.56D$ at 6 diameters downstream.

Although the circular cylinders investigated spanned the reference boundary layer from the momentum thickness ($\delta_{99}/D = 7.86$) to the

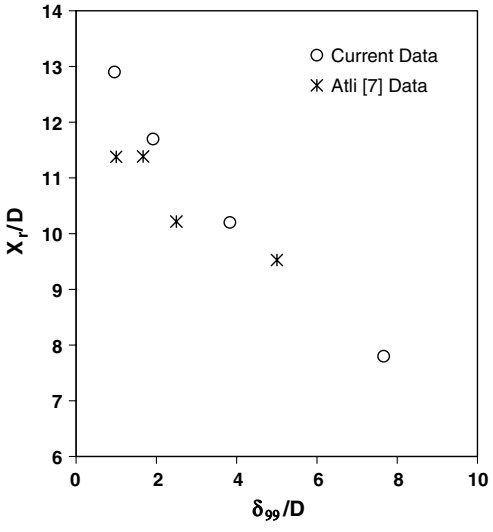

Fig. 13 Recirculation lengths vs δ_{99}/D ratio.

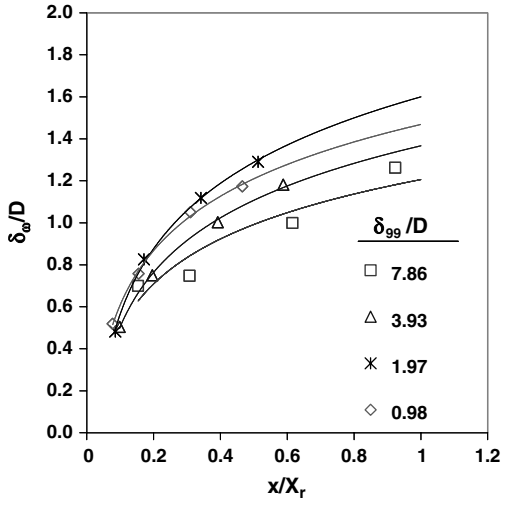

Fig. 14 Shear-layer width in relation to recirculation length.

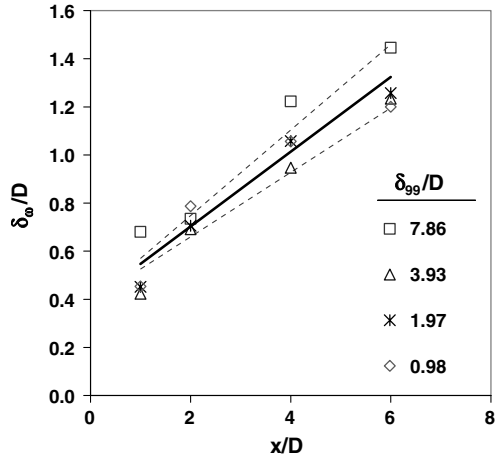

Fig. 15 Shear-layer width in relation to x/D location.

99% thickness ($\delta_{99}/D = 0.98$), the cylinder wakes showed many similarities. In general, all cases were observed to have maximum turbulence-intensity values of 0.17 ± 0.02, which were located at the approximate center of the separated shear layer and found to be independent of downstream position. Furthermore, when normalized by the cylinder diameter, the shear-layer vorticity thickness was found to be independent of the δ_{99}/D ratio, varying linearly with downstream position in terms of cylinder diameter x/D (Fig. 15). The vorticity thickness spread rate (slope of the linear fit in Fig. 15) was calculated to be 0.156, which is comparable with that reported for other free shear flows, in which typical spread rates range from 0.134 to 0.178 [16,17].

Because the ratio of the cylinder diameter to the test-section height was not held constant for the current investigation, blockage effects could be of importance in the reported data. Castro and Fackrell [8] reported that for sharp-edged fence flows, an increasing blockage ratio causes a reduction in the drag coefficient and shorter reattachment length for δ_{99}/D ratios below 2.3, whereas for δ_{99}/D ratios above 2.3, the effects of β are only slight. Furthermore, Siller and Fernholtz [18] noted that blockage effects (again, for sharp-edged fences) are negligible for β less than approximately 11%. Therefore, the effect of blockage should only be observed for the 40 mm cylinder ($\beta = 17\%$). However, when the cylinder size was increased from 20 to 40 mm, C_d decreased but X_r increased (Table 3), which is the opposite of the effect of increasing β reported by Castro and Fackrell [8]. In fact, the only evidence in the current data in which the blockage effect is observed is in Fig. 14, in which δ_ω/D for the 40 mm cylinder is lower than that observed for the 20 mm cylinder. When δ_ω/D was replotted against x/D (Fig. 15), the slight blockage effect observed in Fig. 14 was no longer evident.

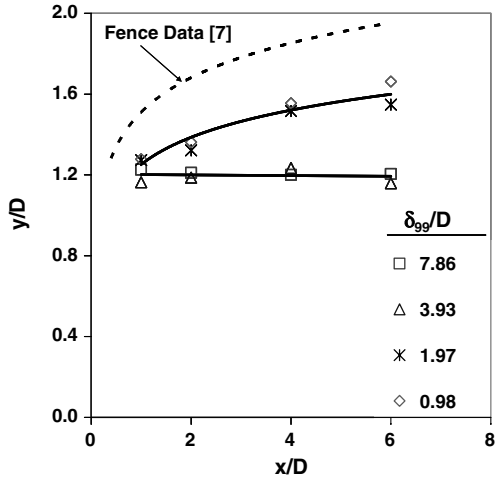

Fig. 16 Shear-layer center location in relation to x/D location.

Therefore, blockage does not appear to have a significant effect on the current results and will be considered to be negligible. A comprehensive study on the effects of blockage on airflow over surface-mounted cylinders is beyond the scope of the current investigation. However, the cutoff value for which blockage effects are negligible for curved obstructions appears to be higher than the 11% previously reported for fences.

Overall, the data show the possibility of the existence of a cutoff δ_{99}/D ratio, below which the separated shear-layer location is suppressed by the high-shear stress in the upstream-approaching boundary layer, causing the shear layer to remain at a relatively predictable constant height. The downstream recirculation region length is therefore only dependent on the spread rate of the shear-layer thickness, which was shown to be independent of δ_{99}/D. This cutoff ratio was found to be on the order of 4, for which the cylinder is one-fourth of the upstream reference boundary-layer thickness. Although this cutoff is best described in a fundamental sense in terms of the obstructed upstream boundary-layer-profile displacement thickness, reference to the unobstructed boundary-layer thickness is better suited for simulator design purposes, in which extensive measurements of the boundary layer with different obstruction sizes are often impractical.

Conclusions

The shear layer separated from various-sized surface-mounted circular cylinders was documented at four downstream locations. Even with a wide range of cylinder sizes examined and the highly curved geometry of the cylinders, the vorticity thickness of the separated shear layer was observed to be a linear function of the downstream location x/D, with spread rates comparable with backward-facing step flows. Furthermore, this observation was found to be independent of the δ_{99}/D ratio, which leads to the conclusion that once the shear layer separates from the cylinder, its growth behavior is similar to other free-shear-layer flows. However, the highly curved geometry of the circular cylinders exhibit previously unreported qualities in the shear-layer trajectory, which in turn affects the downstream recirculation region length.

The shear-layer trajectory was observed by noting the location of the shear-layer center at each downstream location, which was found to be a function of both the downstream distance and the δ_{99}/D ratio. The shear layer for the four cylinders examined was found to follow one of two trajectories: for the two larger cylinders ($\delta_{99}/D = 0.98$ and 1.97), the shear layer was observed to follow a polynomial trajectory, whereas the two smaller cylinders ($\delta_{99}/D = 3.93$ and 7.86) followed a linear trajectory. The polynomial trajectory was found to be similar to sharp-edged fence flows, with fence-flow shear layers reaching a higher trajectory; however, the linear trajectory observed in the current data is previously unreported. The evidence of two independent trajectories in the current data set has not been documented for any surface-mounted geometry and is likely to be attributed to the fact that the separation location on the highly curved surface of the cylinder is free to adjust to boundary conditions, whereas the separation location is fixed on sharp-edged obstructions.

Examination of the effect of the δ_{99}/D ratio on the location of the shear-layer center showed evidence that a cutoff ratio of δ_{99}/D exists to which the location of the separated shear layer will remain constant and independent of downstream location. This cutoff point appears to be on the order of one-fourth of the reference boundary-layer thickness; thus, the shear layer separated from cylinders that are smaller than one-fourth of the boundary layer will maintain constant properties at any downstream location before reattachment. This provides an indication of a possible minimum-size requirement for simulator geometric detail, although further data are required to investigate how these clutter arrangements will affect flame properties. However, these results provide a necessary data set for judgment of the geometric detail required in simulator designs for which previous data do not exist.

Although the data showed some similarities to backward-facing steps and sharp-edged fences, the observations noted previously show that differences are evident for highly curved surface-mounted

obstructions, the current study of which only begins to explain the complexity of this flow configuration. Future investigations into the effect of surface-mounted obstructions on the upstream flow behavior would certainly increase the understanding of this flow phenomenon and aid in the physical interpretation of the 1:4 boundary-layer-to-obstruction ratio, which was found to separate the shear-layer trajectory into two distinct conditions.

Acknowledgments

This work was sponsored by the U.S. Air Force Office of Scientific Research under contract number FA9550-06-C-0031. The views and conclusions contained herein are those of the authors and should not be interpreted as necessarily representing the official policies or endorsements, either expressed or implied, of the U.S. Air Force Office of Scientific Research. The authors would like to thank John Schmisseur at the U.S. Air Force Office of Scientific Research for management of the current project.

References

[1] Bradshaw, P., and Wong, F. Y. K., "The Reattachment and Relaxation of a Turbulent Shear Layer," *Journal of Fluid Mechanics*, Vol. 52, No. 1, 1972, pp. 113–135. doi:10.1017/S002211207200299Xdoi:

[2] Bergeles, G., and Athanassiadis, N., "The Flow Past a Surface Mounted Obstacle," *Journal of Fluids Engineering*, Vol. 105, Dec. 1983, pp. 461–463.

[3] Ke, F., Liu, Y.-Z., Jin, C.-Y., and Wang, W.-Z., "Experimental Measurements of Turbulent Boundary Layer Flow over a Square-Edged Rib," *Journal of Hydrodynamics*, Vol. 18, No. 3, 2006, pp. 461–464. doi:10.1016/S1001-6058(06)60094-2doi:

[4] Archaya, S., Dutta, S., Myrun, T. A., and Baker, R. S., "Turbulent Flow Past a Surface-Mounted Two-Dimensional Rib," *Journal of Fluids Engineering*, Vol. 116, June 1994, pp. 238–246. doi:10.1115/1.2910261

[5] Abdalla, I. E., Cook, M. J., and Yang, Z., "Numerical Study of Transitional Separated-Reattached Flow over Surface Mounted Obstacles Using Large-Eddy Simulation," *International Journal for Numerical Methods in Fluids*, Vol. 54, No. 2, 2007, pp. 175–206. doi:10.1002/fld.1396doi:

[6] Hwang, R. R., Chow, Y. C., and Chiang, T. P., "Numerical Predictions of Turbulent Flow over a Surface-Mounted Rib," *Journal of Engineering Mechanics*, Vol. 125, No. 5, 1999, pp. 497–503. doi:10.1061/(ASCE)0733-9399(1999)125:5(497)doi:

[7] Atli, V., "Subsonic Flow over a Two-Dimensional Obstacle Immersed in a Turbulent Boundary Layer on a Flat Surface," *Journal of Wind Engineering and Industrial Aerodynamics*, Vol. 31, No. 2-3, 1988, pp. 225–239. doi:10.1016/0167-6105(88)90005-0doi:

[8] Castro, I. P., and Fackrell, J. E., "A Note on Two-Dimensional Fence Flows with Emphasis on Wall Constraint," *Journal of Industrial Aerodynamics*, Vol. 3, No. 1, 1978, pp. 1–20. doi:10.1016/0167-6105(78)90025-9doi:

[9] Aragaki, T., Iwata, S., Tange, H., Hiraoka, S., Yamada, I., and Kawaizumi, F., "Theoretical Analysis of Turbulent Flow and Heat Transfer around a Surface Mounted Obstacle," *Journal of Chemical Engineering of Japan*, Vol. 24, No. 2, 1991, pp. 171–177. doi:10.1252/jcej.24.171doi:

[10] Black, A. R., Suo-Anttila, J. M., Disimile, P. J., and Tucker, J. R., "Numerical Predictions and Experimental Results of Air Flow in a Smooth Quarter-Scale Nacelle," 40th AIAA Aerospace Sciences Meeting and Exhibit, AIAA Paper 2002-0856, 2002.

[11] "Improved Temperature Correction in StreamWare," Dantec Dynamics, TN 049909, Skovlunde, Denmark.

[12] Jorgensen, F. E., "Directional Sensitivity of Wire and Fiber-Film Probes," *DISA Information*, Dansk Industri Syndikat, Rept. 11, Herlev, Denmark, 1971.

[13] Wagner, T. C., and Kent, J. C., "On The Dimensional Sensitivity of Hot Wires: A New Look at an Old Approach," *Experiments in Fluids*, Vol. 6, No. 8, Jan. 1988, pp. 553–560.doi:10.1007/BF00196602

[14] Clauser, F. H., "Turbulent Boundary Layers in Adverse Pressure Gradients," *Journal of the Aeronautical Sciences*, Vol. 21, No. 2, 1954, pp. 91–108.

[15] White, F. M., "Incompressible Turbulent Mean Flow," *Viscous Fluid Flow*, 2nd ed., McGraw–Hill, New York, 1991, p. 476.

[16] Brown, G. L., and Roshko, A., "On the Density Effect of Large Structures in Turbulent Mixing Layers," *Journal of Fluid Mechanics*, Vol. 64, No. 4, 1974, pp. 775–816. doi:10.1017/S002211207400190Xdoi:

[17] Viegas, J. R., and Rubesin, M. W., "Assessment of Compressibility Corrections to k-ϵ Model in High Speed Shear Layers," *AIAA Journal*, Vol. 30, No. 10, 1992, pp. 2369–2370. doi:10.2514/3.11235

[18] Siller, H. A., and Fernholz, H., "Separation Behavior in Front of a Two Dimensional Fence," *European Journal of Mechanics, B/Fluids*, Vol. 20, No. 5, 2001, pp 727–740.doi:10.1016/S0997-7546(01)01153-0

F. Coton
Associate Editor